Tungsten in barium stars

M. P. Roriz [1]★ M. Lugaro,[2,3,4,5] S. Junqueira,[1] C. Sneden,[6] N. A. Drake [1,7] and C. B. Pereira[1]

[1]*Observatório Nacional/MCTI, Rua General José Cristino, 77, 20921-400, Rio de Janeiro, Brazil*

[2]*Konkoly Observatory, HUN-REN Research Centre for Astronomy and Earth Sciences, H-1121 Budapest, Konkoly Thege M. út 15-17, Hungary*

[3]*CSFK, MTA Centre of Excellence, H-1121 Budapest, Konkoly Thege Miklós út 15-17, Hungary*

[4]*ELTE Eötvös Loránd University, Institute of Physics, Budapest 1117, Pázmány Péter sétány 1/A, Hungary*

[5]*School of Physics and Astronomy, Monash University, VIC 3800, Australia*

[6]*Department of Astronomy and McDonald Observatory, The University of Texas, Austin, TX 78712, USA*

[7]*Laboratory of Observational Astrophysics, Saint Petersburg State University, Universitetski pr. 28, 198504 Saint Petersburg, Russia*

ABSTRACT

Classical barium stars are red giants that receive from their evolved binary companions material exposed to the *slow* neutron-capture nucleosynthesis, i.e. the *s*-process. Such a mechanism is expected to have taken place in the interiors of Thermally-Pulsing Asymptotic Giant Branch (TP-AGB) stars. As post-interacting binaries, barium stars figure as powerful tracers of the *s*-process nucleosynthesis, evolution of binary systems, and mechanisms of mass transfer. The present study is the fourth in a series of high-resolution spectroscopic analyses on a sample of 180 barium stars, for which we report tungsten (W, $Z = 74$) abundances. The abundances were derived from synthetic spectrum computations of the W I absorption features at 4843.8 and 5224.7 Å. We were able to extract abundances for 94 stars; the measured [W/Fe] ratios range from ∼0.0 to 2.0 dex, increasing with decreasing metallicity. We noticed that in the plane [W/Fe] versus [*s*/Fe], barium stars follow the same trend observed in post-AGB stars. The observational data were also compared with predictions of the FRUITY and Monash AGB nucleosynthesis models. These expect values between -0.20 and $+0.10$ dex for the [W/hs] ratios, whereas a larger spread is observed in the program stars, with [W/hs] ranging from -0.40 to $+0.60$ dex. The stars with high [W/hs] ratios may represent evidence for the operation of the intermediate neuron-capture process at metallicities close to solar.

Key words: nuclear reactions, nucleosynthesis, abundances – stars: abundances – stars: AGB and post-AGB – stars: chemically peculiar.

1 INTRODUCTION

A large fraction of elements beyond the iron-peak ($Z > 30$) is produced in the interiors of Thermally-Pulsing Asymptotic Giant Branch stars (TP-AGB; Gallino et al. 1998; Straniero, Gallino & Cristallo 2006; Karakas & Lattanzio 2014) through the *slow* neutron-capture mechanism (*s*-process; Käppeler et al. 2011; Lugaro et al. 2023). From convective mixing episodes, the newly synthesized nuclei are brought to the stellar surface, changing the chemical composition of the star. Subsequently, the enriched material is ejected to the interstellar medium via stellar mass-loss events. In addition to *s*-elements, AGB stars can also play an important role in the Galactic chemical evolution of C, N, and F (e.g. Kobayashi, Karakas & Lugaro 2020). Generally, these objects are observed as S-type stars. Indeed, the detection of the radioactive ^{99}Tc on their atmospheres (Merrill 1952) provided an unambiguous observational evidence that the *s*-process nucleosynthesis is on-going within these stars.

On the other hand, observations also show that about 50 per cent of S-type stars do not show Tc absorption features in their spectra (see Van Eck, Shetye & Siess 2022). These outlier stars are probably

first ascent giants, therefore unable to internally produce the heavy elements observed in their envelopes. In fact, they are thought to be members of post-interacting binary systems, where mass transfer took place and their chemical peculiarities originated (e.g. Jorissen et al. 1998, 2019). In that framework, the observed stars received from their evolved companion the *s*-processed material. Thus, they are referred to as *extrinsic*, instead of being *intrinsic* S stars. The *s*-rich sub-class of the Carbon-Enhanced Metal-Poor stars (i.e. CEMP-*s*; Beers & Christlieb 2005), giant CH stars (Keenan 1942), and classical barium stars (Bidelman & Keenan 1951) are representative of such extrinsic stars.

The classical barium stars are the warmest extrinsic *s*-rich stars; they are G/K spectral-type giants with effective temperatures ranging from 4000 to 6000 K. The abnormal strengthening of the Ba II and Sr II absorption lines, along with the relatively intense CH, CN, and C_2 molecular bands observed in their spectra posed a challenge to early stellar evolution models. McClure, Fletcher & Nemec (1980) first reported radial velocity variations in these systems and shed light on the binary nature of barium stars. Over the years, such a scenario has been confirmed and extensively explored from data of radial velocity monitoring programs (Jorissen & Mayor 1988; Jorissen et al. 1998; Escorza et al. 2019; Jorissen et al. 2019; Escorza & De Rosa 2023). As post-interacting binary systems, the

★ E-mail: michelle@on.br

orbital elements of barium stars have provided valuable observational constraints to binary evolution models, as well as clues on mass transfer mechanisms.

Beginning with the first quantitative abundance analysis of the barium star HD 46407 (Burbidge & Burbidge 1957), many studies have found moderated carbon enhancements ([C/Fe] ≈ 0.30)[1] and *s*-process average abundances that can reach values [*s*/Fe] > 1.0 in barium stars. Although a lower limit in the [*s*/Fe] index to categorize an object as a barium star is not well established, de Castro et al. (2016) suggested [*s*/Fe] > 0.25. Irrespective of the degree of C and *s*-enhancement observed in various barium stars, they figure as powerful *s*-process tracers of their cooler counterparts (i.e. intrinsic S-stars), providing strong constraints to the nucleosynthesis models (e.g. Allen & Barbuy 2006a, b; Smiljanic, Porto de Mello & da Silva 2007; Pereira et al. 2011; de Castro et al. 2016; Yang et al. 2016; Cseh et al. 2018; Karinkuzhi et al. 2018; Shejeelammal et al. 2020; Roriz et al. 2021a, b; Cseh et al. 2022). To trace back the envelope abundances of a barium star to the former TP-AGB companion, now quietly orbiting it as a dim white dwarf, it is important to explore all available elemental abundances on its atmosphere.

The present paper is the fourth in a series of studies started by de Castro et al. (2016, hereafter Paper I), who conducted a chemical and kinematic analysis for a large sample of barium giant stars based on high-resolution spectroscopic data. In Paper I, ∼180 targets were subjected to statistical analysis. Later, Rb abundances were extracted for these stars in Roriz et al. (2021a, hereafter Paper II), since Rb is a key element to constrain the neutron source of the *s*-process (see van Raai et al. 2012). In Paper II, we found [Rb/Zr] < 0 for these systems. In the light of theoretical *s*-process nucleosynthesis models, this is expected when ^{13}C acts as the main neutron source of the *s*-process (Gallino et al. 1998). In other words, Paper II provided an additional evidence for the low-mass nature (i.e. ≲3 M$_\odot$) of the former AGB stars that contaminated the envelopes of the observed barium stars. In Roriz et al. (2021b, hereafter Paper III), we re-derived the La abundances previously reported in Paper I, and extracted new abundances for other neutron-capture (*n*-) elements, namely Sr, Nb, Mo, Ru, Sm, and Eu. Most importantly, for the elements Nb, Mo, and Ru, which are nuclei between the first (Sr, Y, Zr) and second (Ba, La, Ce) *s*-process peaks, the observations were at odds with nucleosynthesis models. We found abundances systematically higher than theoretical predictions from the *s*-process, which led us to suggest alternative nucleosynthesis paths to interpret the observations (see also Cseh et al. 2022; den Hartogh et al. 2023).

In the present study, we aim to extend the abundance pattern of barium stars by evaluating tungsten (W, $Z = 74$) abundances in our sample of 180 barium giants. As far as we are aware, W stellar abundances (or upper limits) have been reported in the literature just for a few sources: the barium star HD 46407 (Burbidge & Burbidge 1957), 8 post-AGB stars (Reyniers & Van Winckel 2003; Reyniers et al. 2004; De Smedt et al. 2012; van Aarle et al. 2013; De Smedt et al. 2016), and 5 metal-poor ([Fe/H] ≲ −1.50) stars (Siqueira Mello et al. 2013; Roederer et al. 2014, 2016, 2022). More recently, Roriz et al. (2023) derived W abundances in 1 new barium giant (HE 0457-1805), 1 new CH star (HE 1255-2324), and 1 probable CH star (HE 2207-1746). W is an element located between the second and third (Pb) *s*-process peaks, and its solar abundance is predicted to have a contribution of 62 per cent from the *s*-process (Bisterzo et al. 2014).

The abundance of W produced by the *s*-process mostly follows that of the second peak at Ba and La and can be used as a diagnostic of the neutron flux (see, e.g. Reyniers & Van Winckel 2003). For example, Lugaro et al. (2015) demonstrated that the relatively high W and low Pb abundances in post-AGB stars cannot be explained by the *s*-process, which calls for the intermediate (*i*-) neutron-capture process (Cowan & Rose 1977) to be responsible for the observed pattern.

The paper is organized as follows. In Section 2, we provide a summary of the target stars. In Section 3, we describe the approach in deriving W abundances and estimating their uncertainties. We discuss the novel results in Section 4, and analyse the data set in the light of the *s*-process nucleosynthesis models in Section 5. Finally, in Section 6, we draw our conclusions.

2 PROGRAM STARS

The program stars comprise 166 sources of Paper I, 11 metal-rich ([Fe/H] ≥ 0.10) barium stars previously analysed by Pereira et al. (2011), two barium stars identified by Katime Santrich, Pereira & de Castro (2013) in the open cluster NGC 5822 (#2 and #201), and the barium star HD 10613 from Pereira & Drake (2009). Therefore, a total of 180 targets. The atmospheric parameters adopted here are the same previously adopted in Papers II and III. For completeness, they are shown in Table A1. In summary, these stars were observed between the years 1999 and 2010, and their high-resolution spectra were acquired with the Fiber-fed Extended Range Optical Spectrograph (FEROS; Kaufer et al. 1999) attached to the 1.52 and 2.2 m ESO telescopes at La Silla (Chile). The instrument has a spectral coverage within the range from ∼3900 to 9200 Å with a resolving power $R = \lambda/\Delta\lambda \sim 48\,000$.

3 ABUNDANCE ANALYSIS

3.1 Abundance derivation

As previously mentioned, W abundances have been reported so far only for 17 stars. In addition to the limited number of useful diagnostic lines, spectral blends make difficult the task of deriving the chemical abundance of W. Previous works, based on near-ultraviolet spectra of metal-poor stars, reported W abundances from eight W II lines, mainly the transitions at 2088.204 and 2118.875 Å (see Siqueira Mello et al. 2013; Roederer et al. 2014, 2016, 2022). In the optical window, the W I line at 5053.280 Å (van Aarle et al. 2013) and the W II line at 5104.432 Å (Reyniers & Van Winckel 2003; Reyniers et al. 2004; De Smedt et al. 2012, 2016) were detected in the spectra of post-AGB stars. Recently, also in the optical domain, Roriz et al. (2023) used two absorption features of W I centred at 4843.810 and 5224.661 Å to derive W abundances for the stars HE 0457-1805, HE 1255-2324, and HE 2207-1746 already mentioned in the Introduction.

To extract W abundances in the program stars, we have followed the same approach carried out by Roriz et al. (2023). In other words, we fitted synthetic spectra to the W I features at 4843.810 and 5224.661 Å. To model the theoretical spectra, we run the *synth* drive of the radiative-transfer code MOOG (Sneden 1973; Sneden et al. 2012), which assumes a plane–parallel stellar atmosphere and the Local Thermodynamic Equilibrium (LTE) conditions. To compute the synthetic spectra, MOOG needs as inputs an atmospheric model and a linelist containing the lab data of relevant transitions in that spectral region. We have also adopted here the 1D plane–parallel model atmospheres of Kurucz (1993), as done in previous papers.
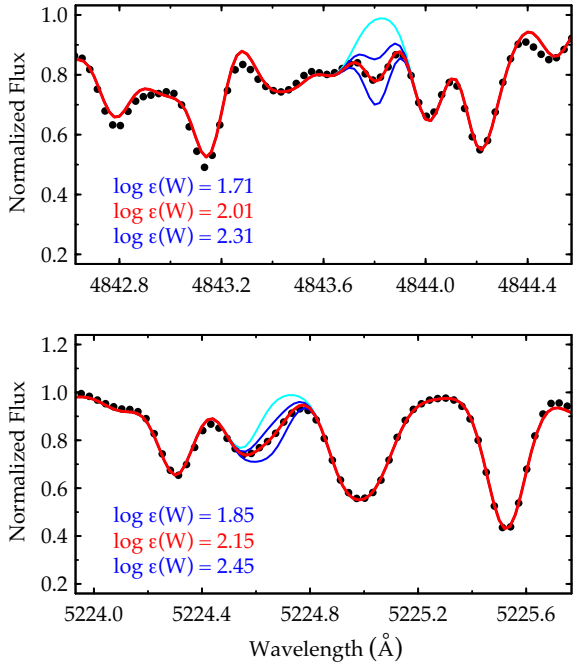
Figure 1. A portion of the spectral region around the W I lines at 4843.8 Å (top panel) and 5224.6 Å (bottom panel). The black dots represent the observed spectrum of the star HD 107541, and the curves are synthetic spectra computed for different W abundances, as indicated in each panel. The best-fit syntheses are shown in red, whereas the blue curves are spectra computed for $\Delta \log \epsilon(W) = \pm 0.3$ around the adopted solution. In cyan, we show theoretical spectra computed without W contribution.

For the W lines, we adopted the line parameters provided by the Vienna Atomic Line Database (VALD; Ryabchikova et al. 2015). The transition at 4843.810 Å has an excitation potential $\chi = 0.412$ eV and $\log gf = -1.54$, while the other at 5224.661 Å has $\chi = 0.599$ eV and $\log gf = -1.70$. Tungsten has five stable isotopes, among which only the ^{183}W presents a non-zero nuclear spin ($I = 1/2$); however, hyperfine structure data are not available for that nuclide.

In Fig. 1, we show as an example the spectral regions close to the two W I lines observed for the star HD 107541, as well as synthetic spectra computed for different W abundances. Note that the W I line at 4843.8 Å is clearly present in the spectrum of this star, as shown in the upper panel of the figure. On the other hand, as seen in the lower panel of Fig. 1, the absorption at 5224.6 Å is a blended feature; however, to fit the observation, the contribution of W I at 5224.661 Å in the spectral synthesis computations is necessary. In Table A1, we provide the abundances derived from each line for the target stars, as well as the adopted values in this work. A further inspection of Table A1 shows that abundances derived from the two W I lines agree reasonably well, which confirms the reliability of the tungsten determination in our sample of barium stars. Tungsten abundances were derived for a total of 94 out of the 180 stars analysed here. All of these, except one (HD 88562), exhibited in their spectra the line at 4843.810 Å, whereas the line at 5224.661 Å was detected in 73 of them. For the other 86 program stars, the two W I lines were absent or weakly detectable, so that abundances were not evaluated. Temperature and the degree of s-enrichment are two relevant factors for the appearance of the W I lines in the spectra of the target stars. This follows directly from the Saha–Boltzmann formulas, as well as the fact that the line intensity grows with the increase of atmospheric W abundance.

For the chemical species considered in Papers I, II, and III, the recommendations of Grevesse & Sauval (1998) for the solar photosphere abundances were systematically used. Such an assumption implies in a mean difference of -0.04 ± 0.04 with respect to the updated values of Asplund et al. (2009). On the other hand, as far as W is concerned, its solar photosphere abundance reported by Grevesse & Sauval, $\log \epsilon(W)_\odot = 1.11$, is flagged as less accurate, and a much lower meteorite value is recommended by these authors, namely $\log \epsilon(W)_\odot = 0.65$. The recommendations of Asplund et al. (2009) for the solar photosphere and meteorite abundances are $\log \epsilon(W)_\odot = 0.85$ and 0.65, respectively, and also present an offset, but in a lesser extent than in Grevesse & Sauval. Thus, in view of that issue and to perform a fair comparison with theoretical predictions (Section 5), which are computed from meteorite abundances, we have adopted in this work the meteorite value of 0.65, the same value adopted in the nucleosynthesis models. For consistency, we have also normalized the data compiled from the literature to that value.

3.2 Uncertainty estimates

To evaluate the uncertainties associated to the W abundances, we have grouped the stars into three ranges of effective temperatures. In Group 1, we selected stars with temperatures between 5000 and 5400 K; in Group 2, stars with 4700 and 4950 K; in Group 3, stars with 4100 and 4600 K. In our previous studies, the stars BD $-14°2678$, HD 119185, and HD 130255 were taken as templates of Groups 1, 2, and 3, respectively. However, as the W lines were weakly detectable in these targets, they were replaced by the stars HD 114678, HD 29370, and HD 211954, respectively.

By varying the atmospheric parameters, i.e. effective temperature ($T_{\rm eff}$), surface gravity ($\log g$), microturbulent velocity (ξ), and metallicity ([Fe/H]), we computed the corresponding changes introduced in $\log \epsilon(Fe)$ and $\log \epsilon(W)$. Additionally, to take into account the random error ($\sigma_{\rm ran}$) due to continuum uncertainties, we computed the minimal abundance variations for which a clear visual difference is seen between the synthetic and observed spectra. The total uncertainties in $\log \epsilon(Fe)$ and $\log \epsilon(W)$ for the template stars were estimated by adding quadratically the changes introduced in abundance and extracting the root square. In this approach, we assume that the errors are independent. The total abundance uncertainties are shown in the last column of Table 1. These values were applied to the objects of the respective subsample, as shown in Table A1. Finally, for the [W/Fe] ratios, the uncertainties were estimated according to the relationship $\sigma_{[W/Fe]}^2 = \sigma_W^2 + \sigma_{Fe}^2$.

4 DISCUSSION

In Fig. 2, we plot the [W/Fe] ratios observed in our barium giants (grey dots) as a function of metallicity. We found W abundances spanning within the interval $0.0 \lesssim [W/Fe] \lesssim +2.0$. Data for [W/Fe] available in the literature for post-AGB stars, metal-poor stars, and other chemically peculiar systems are also added in the same plot as black symbols; these are properly identified in the figure caption. As Fig. 2 shows, five W abundances are available for metal-poor stars, among which three are upper limits for the [W/Fe] ratios. The data do not evidence any trend for [Fe/H] $\lesssim -1.50$. Additionally, in this metallicity range, s-process nucleosynthesis is not expected to play a significant role. Indeed, the Galactic chemical evolution (GCE) models of Kobayashi, Karakas & Lugaro (2020), performed for elements from C to U, predict [W/Fe] ~ 0.40, if contributions from magnetorotational supernovae are taken into account (see Fig. 2); otherwise, values close to [W/Fe] ~ -0.70 are predicted.

Table 1. Abundance uncertainty estimates for the template stars HD 114678, HD 29370, and HD 211954, performed for the elements iron and tungsten. Columns from 2 to 6 give the variations introduced in abundances owing by changes in T_{eff}, $\log g$, ξ, [Fe/H], and equivalent width measurements (W_λ), respectively. Column 7 gives the random errors. Finally, the composed uncertainties are shown in Column 8.

Species	ΔT_{eff}	$\Delta \log g$	$\Delta \xi$	Δ[Fe/H]	ΔW_λ [a]	σ_{ran} [b]	$\sqrt{\Sigma \sigma^2}$
			Group 1 – HD 114678				
	(+100 K)	(+0.2 dex)	(+0.3 km s^{-1})	(+0.1 dex)	(+3 mÅ)		
Fe I	+0.10	0.00	−0.11	−0.01	+0.06	0.02	0.16
W I	+0.23	0.00	0.00	0.00	–	0.20	0.30
			Group 2 – HD 29370				
	(+100 K)	(+0.2 dex)	(+0.3 km s^{-1})	(+0.1 dex)	(+3 mÅ)		
Fe I	+0.08	+0.01	−0.13	0.00	+0.05	0.02	0.16
W I	+0.20	+0.03	0.00	+0.03	–	0.15	0.25
			Group 3 – HD 211954				
	(+90 K)	(+0.2 dex)	(+0.3 km s^{-1})	(+0.1 dex)	(+3 mÅ)		
Fe I	+0.03	+0.02	−0.16	+0.02	+0.06	0.03	0.18
W I	+0.18	+0.03	−0.20	+0.03	–	0.18	0.33

Note. [a] Evaluated only for the iron lines, from data of Paper I. [b] For the iron lines, σ_{ran} is evaluated as $\sigma_{obs}/\sqrt{N}$, where σ_{obs} is the standard deviation and N is the number of iron lines used, from data of Paper I.
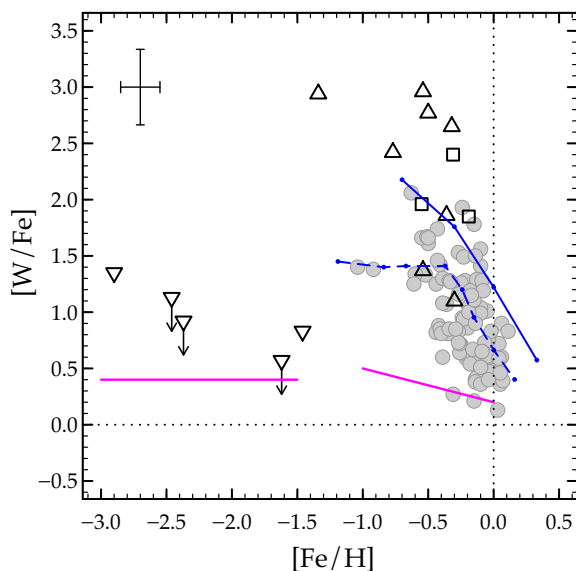

Figure 2. Tungsten-to-iron abundance ratios observed in barium giant stars (grey dots) as a function of metallicity. For the sake of clarity, only a typical error bar of data set is shown. Black symbols are data reported in the literature for metal-poor stars (inverted triangles; from Siqueira Mello et al. 2013; Roederer et al. 2014, 2016, 2022), post-AGB stars (up triangles; from Reyniers & Van Winckel 2003; Reyniers et al. 2004; De Smedt et al. 2012; van Aarle et al. 2013; De Smedt et al. 2016), and other chemically peculiar stars (squares; from Roriz et al. 2023). As far as we are aware, no other stellar W abundances have been reported in the literature in addition to these data. The magenta lines mimic the GCE models computed by Kobayashi, Karakas & Lugaro (2020), as seen in their fig. 32. Blue curves are some examples of theoretical expectations of the *s*-process for TP-AGB stars of 3.0 M$_\odot$ computed by the Monash group (solid line) and FRUITY data base (dashed line); these models will be discussed in Section 5.

For [Fe/H] > -1.0, the data shown in Fig. 2 reflect directly the *s*-process nucleosynthesis. This is noticeable by the [W/Fe] ratios decreasing with increasing [Fe/H], a typical feature of the *s*-process (Busso et al. 2001; Cseh et al. 2018). Post-AGB stars typically show the highest [W/Fe] values. For normal field stars in this metallicity range, W abundances are not available. Examples of theoretical
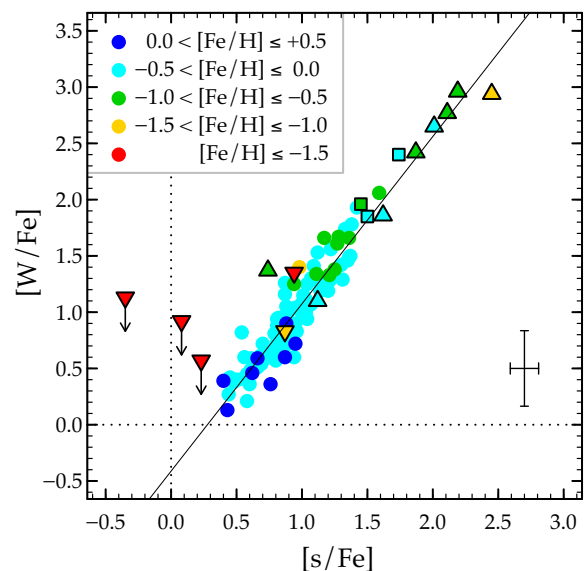
Figure 3. [W/Fe] ratios against [*s*/Fe] for the program stars (colour dots), along with data from the literature. The symbols have the same meaning as in Fig. 2, however, as shown in the top of panel, we adopted here a code colour in order to identify the different metallicity regimes of the stars. For the sake of clarity, only a typical error bar is shown. The black straight line is a linear fit of data observed in barium giants.

[W/Fe] ratios, expected by AGB nucleosynthesis models of 3 M$_\odot$ and able to reach [*s*/Fe] > 0.25, are also shown in Fig. 2 (blue curves). They are plotted in this figure only to illustrate how much W these models are able to produce. They should not be compared directly with our observational data set, since the material received by the barium stars is further diluted on their convective envelopes. These models will be discussed in detail in Section 5.

In Fig. 3, the [W/Fe] ratios are plotted as a function of the *s*-process mean abundance, denoted by the [*s*/Fe] index. This index is evaluated as the average of [X/Fe] ratios derived for the Sr, Y, Zr, La, Ce, and Nd – elements of the first and second *s*-process peaks. The [*s*/Fe] values are given in the last column of Table A1 and lie in the range of +0.23

$\leq$ [*s*/Fe] $\leq$ +1.59.[2] As previously mentioned, there is no consensus concerning the lower limit for the [*s*/Fe] index to consider an object as a barium star. We have adopted here the condition [*s*/Fe] $\geq$ 0.25 dex assumed in Papers I, II, and III. We have also observed that for barium stars with [*s*/Fe] <0.40 dex, the two W I lines are not detectable in their spectra (see also Table A1). Fig. 3 clearly demonstrates the strong correlation between [W/Fe] and [*s*/Fe] (as well as [Fe/H]) observed in our barium stars. Such a correlation confirms that W is produced within the former polluting TP-AGB stars, since the *s*-process enrichment levels are accompanied by higher W abundances. A least square fitting of the data set provides a relationship given by [W/Fe] = (1.49 ± 0.06) × [*s*/Fe] − (0.41 ± 0.06). Interestingly, we note that the sources previously investigated in the literature fall very closely the linear fit, except for the metal-poor stars HD 108317, HD 128279, and HD 94028, for which only upper limits could be determined (Roederer et al. 2014, 2016).

5 COMPARISON TO NUCLEOSYNTHESIS MODELS

AGB stars experience thermal instabilities and dredge-up episodes, which, in turn, favour nucleosynthesis via *s*-process (Gallino et al. 1998; Busso, Gallino & Wasserburg 1999; Busso et al. 2001; Straniero, Gallino & Cristallo 2006; Karakas & Lattanzio 2014; Lugaro et al. 2023). Between the He- and H-burning shells, which are alternately activated in the TP-AGB phase, there is a small intershell region ($\sim$10^{-2} M$_\odot$) rich in He and C, where the *s*-process nucleosynthesis takes place. For low-mass stars, the ^{13}C(α, *n*)^{16}O reaction provides the major neutron reservoir of the *s*-process. This reaction is activated at $T \sim 10^8$ K in radiative conditions during the H-burning shell (interpulse period) (Straniero et al. 1995; Gallino et al. 1998). The other neutron source, the ^{22}Ne(α, *n*)^{25}Mg reaction, does not play a relevant role as neutron source for this mass range. It is marginally activated at $T \sim 3 \times 10^8$ K, during the brief and recurrent He-burning shell episodes (thermal-pulse; TP), which temporarily extinguish the H fusion. Additionally, the CNO cycle in the H-burning shell does not leave in the intershell the required ^{13}C amounts to drive the *s*-process (Gallino et al. 1998). Therefore, to model the nucleosynthesis of heavy elements, a partial mixing zone is assumed in the top layers of intershell, allowing the penetration of protons from the convective envelope during the third dredge-up (TDU) episodes. These protons are combined with the ^{12}C nuclei present there to form a ^{13}C pocket, where ^{13}C burns in the next interpulse. However, the exact mechanism that leads to the formation of the ^{13}C pocket in the intershell is not well understood, which introduces the major uncertainty source in predictions (see, e.g. Karakas & Lattanzio 2014; Lugaro et al. 2023).

Theoretical predictions for the *s*-process yields produced in TP-AGB stars for a wide range of masses (1.0 < *M*/M$_\odot$ < 8.0) and metallicities ($-1.2 \lesssim$ [Fe/H] $\lesssim$ +0.3) are tabulated and made publicly available by the INAF group (Cristallo et al. 2009, 2011, 2015), through the FRUITY[3] data base, and the Monash group (Fishlock et al. 2014; Karakas & Lugaro 2016; Karakas et al. 2018). Since that metallicity range covers the interval observed in barium
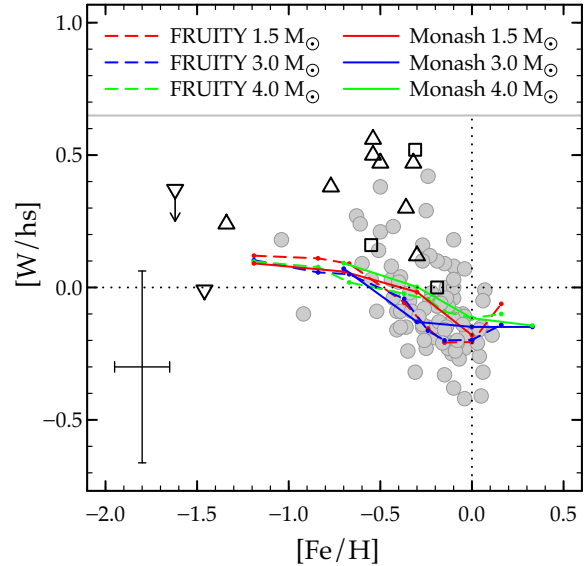

Figure 4. [W/hs] ratios observed in barium giant stars as a function of metallicity. The observations are compared to predictions from the Monash (continuous line) and FRUITY (dashed lines) nucleosynthesis models for AGB of initial masses of 1.5, 3.0, and 4.0 M$_\odot$. Data for metal-poor stars and post-AGB stars are also shown in the plot. Symbols have the same meaning as in Fig. 2.

stars, we examine our observations in light of these two sets of *s*-process nucleosynthesis models. Because the abundance profiles observed in barium stars have evidenced the most likely low-mass ($M \lesssim 3.0$ M$_\odot$) nature of their former polluting TP-AGB stars (e.g. Cseh et al. 2018; Karinkuzhi et al. 2018; Shejeelammal et al. 2020; Cseh et al. 2022; Paper II; Paper III), we concentrate our attention in (non-rotating) models of masses equal to 1.5, 3.0, and 4.0 M$_\odot$.

A careful comparison between FRUITY and Monash models, highlighting their similarities and differences, is provided by Karakas & Lugaro (2016), to which we refer the reader. Generally speaking, in the FRUITY models, the ^{13}C pocket is generated via a time-dependent convective overshoot implementation (Cristallo et al. 2009). In the Monash models, instead, a post-processing is performed to compute the detailed nucleosynthesis. In this step, the ^{13}C pocket is formed from a parametric approach, in which a mass of protons (M_{mix}) is artificially inserted in the top layers of the intershell during the TDU (Karakas & Lugaro 2016). Additionally, different physical and nuclear inputs are used in the FRUITY and Monash models. We have selected here only the models with the standard choice of the mass of ^{13}C pocket, able to reach [*s*/Fe] > 0.25. We then compare our observations with predictions computed at the stellar surface at the end of the AGB evolution.

In Fig. 2, models of 3.0 M$_\odot$ are shown as examples. Note that they are able to produce [W/Fe] ratios increasing from $\sim$0.5 to $\sim$2.2 with decreasing metallicities. As we previously mentioned, the predicted [W/Fe] ratios cannot be directly compared to observations, since the models do not account for the mass transfer and the further dilution of the *s*-processed material in the atmospheres of barium stars. In any case, the predictions behave similarly to the observations, since dilution has the effect of lowering the predicted W abundances but without changing the shape of the distribution (see, e.g. Cseh et al. 2022). In order to eliminate dilution effects and compare theoretical predictions with observations, we evaluated ratios between elements from different *s*-process peaks. In Fig. 4, we plot the ratios [W/hs] =

[W/Fe] − [hs/Fe] as a function of metallicity, where [hs/Fe] denotes the average abundance of the elements La, Ce, and Nd, belonging to the second *s*-process peak. As shown in this figure, the [W/hs] ratios observed in barium stars span between −0.40 and +0.60, and most of the stars (∼90 per cent of the targets for which W abundances were evaluated) exhibit [W/hs] < 0. The *s*-process model results are mostly controlled by the relatively well-known neutron-capture cross-sections of the isotopes involved. Predicted trends show mild variations, of up to +0.3 dex when decreasing [Fe/H], and are not able to cover the full observational spread. Some of this spread may be attributed to the observational error bars, however, there are a few data points that show significant excesses of W. These may be interpreted as a signature of the *i*-process (see Lugaro et al. 2015).

6 CONCLUSIONS

We have reported new observational data of tungsten abundances for a sample of 180 barium giant stars. So far, abundances (or upper limits) of this element are found in the literature only for 17 targets. Based on the LTE assumptions, W abundances were derived for 94 barium stars via spectral synthesis of two W I absorption features centred at 4843.8 and 5224.7 Å. For the remaining 86 stars of the sample, these two W I lines were either absent or weakly detectable in their spectra. We found [W/Fe] ratios spanning from ∼0.0 to 2.0 dex, increasing for lower metallicities, and with typical uncertainties of the order of ±0.30 dex. As discussed, such abundances cannot be explained as a consequence of the GCE. In fact, GCE models predict no more than +0.50 dex (Kobayashi, Karakas & Lugaro 2020). The strong correlation between the [W/Fe] and [*s*/Fe] ratios observed in the atmospheres of program barium stars evidences that the W was produced by the *s*-process nucleosynthesis. We also noticed that in the plane [W/Fe] versus [*s*/Fe] barium stars follow the same trend observed in post-AGB stars, as shown in Fig. 3. Finally, the [W/hs] ratios were compared with predictions from the FRUITY and Monash nucleosynthesis models, which expect −0.20 < [W/hs] < +0.10. We found that the *s*-process models are able to reproduce the bulk of observations, although the spread of the data set is greater than predictions, as seen in Fig. 4. Higher [W/hs] than predicted may be the signature of the *i*-process, especially in connection to lower than expected [Pb/hs] abundances. Further data on the other elements located just before or at the third *s*-process peak will shed more light on this possibility and may provide evidence for the existence of the *i*-process at metallicities close to solar.

DATA AVAILABILITY

The data underlying this article are available in the article.

REFERENCES

Allen D. M., Barbuy B., 2006a, A&A, 454, 895
Allen D. M., Barbuy B., 2006b, A&A, 454, 917
Asplund M., Grevesse N., Sauval A. J., Scott P., 2009, ARA&A, 47, 481
Beers T. C., Christlieb N., 2005, ARA&A, 43, 531
Bidelman W. P., Keenan P. C., 1951, ApJ, 114, 473
Bisterzo S., Travaglio C., Gallino R., Wiescher M., Käppeler F., 2014, ApJ, 787, 10
Burbidge E. M., Burbidge G. R., 1957, ApJ, 126, 357
Busso M., Gallino R., Wasserburg G. J., 1999, ARA&A, 37, 239
Busso M., Gallino R., Lambert D. L., Travaglio C., Smith V. V., 2001, ApJ, 557, 802
Cowan J. J., Rose W. K., 1977, ApJ, 212, 149
Cristallo S., Straniero O., Gallino R., Piersanti L., Domínguez I., Lederer M. T., 2009, ApJ, 696, 797
Cristallo S. et al., 2011, ApJS, 197, 17
Cristallo S., Straniero O., Piersanti L., Gobrecht D., 2015, ApJS, 219, 40
Cseh B. et al., 2018, A&A, 620, A146
Cseh B. et al., 2022, A&A, 660, A128
de Castro D. B., Pereira C. B., Roig F., Jilinski E., Drake N. A., Chavero C., Sales Silva J. V., 2016, MNRAS, 459, 4299
den Hartogh J. W. et al., 2023, A&A, 672, A143
De Smedt K., Van Winckel H., Karakas A. I., Siess L., Goriely S., Wood P. R., 2012, A&A, 541, A67
De Smedt K., Van Winckel H., Kamath D., Siess L., Goriely S., Karakas A. I., Manick R., 2016, A&A, 587, A6
Escorza A., De Rosa R. J., 2023, A&A, 671, A97
Escorza A. et al., 2019, A&A, 626, A128
Fishlock C. K., Karakas A. I., Lugaro M., Yong D., 2014, ApJ, 797, 44
Gallino R., Arlandini C., Busso M., Lugaro M., Travaglio C., Straniero O., Chieffi A., Limongi M., 1998, ApJ, 497, 388
Grevesse N., Sauval A. J., 1998, Space Sci. Rev., 85, 161
Jorissen A., Mayor M., 1988, A&A, 198, 187
Jorissen A., Van Eck S., Mayor M., Udry S., 1998, A&A, 332, 877
Jorissen A., Boffin H. M. J., Karinkuzhi D., Van Eck S., Escorza A., Shetye S., Van Winckel H., 2019, A&A, 626, A127
Käppeler F., Gallino R., Bisterzo S., Aoki W., 2011, Rev. Mod. Phys., 83, 157
Karakas A. I., Lattanzio J. C., 2014, PASA, 31, e030
Karakas A. I., Lugaro M., 2016, ApJ, 825, 26
Karakas A. I., Lugaro M., Carlos M., Cseh B., Kamath D., García-Hernández D. A., 2018, MNRAS, 477, 421
Karinkuzhi D. et al., 2018, A&A, 618, A32
Katime Santrich O. J., Pereira C. B., de Castro D. B., 2013, AJ, 146, 39
Kaufer A., Stahl O., Tubbesing S., Nørregaard P., Avila G., Francois P., Pasquini L., Pizzella A., 1999, The Messenger, 95, 8
Keenan P. C., 1942, ApJ, 96, 101
Kobayashi C., Karakas A. I., Lugaro M., 2020, ApJ, 900, 179
Kurucz R., 1993, ATLAS9 Stellar Atmosphere Programs and 2 km/s grid. Kurucz CD-ROM No. 13. Smithsonian Astrophysical Observatory, Cambridge, p. 13
Lugaro M., Campbell S. W., Van Winckel H., De Smedt K., Karakas A. I., Käppeler F., 2015, A&A, 583, A77
Lugaro M., Pignatari M., Reifarth R., Wiescher M., 2023, Annu. Rev. Nucl. Part. Sci., 73, 315
McClure R. D., Fletcher J. M., Nemec J. M., 1980, ApJ, 238, L35
Merrill P. W., 1952, ApJ, 116, 21
Pereira C. B., Drake N. A., 2009, A&A, 496, 791
Pereira C. B., Sales Silva J. V., Chavero C., Roig F., Jilinski E., 2011, A&A, 533, A51
Reyniers M., Van Winckel H., 2003, A&A, 408, L33
Reyniers M., Van Winckel H., Gallino R., Straniero O., 2004, A&A, 417, 269

Roederer I. U. et al., 2014, ApJ, 791, 32

Roederer I. U., Karakas A. I., Pignatari M., Herwig F., 2016, ApJ, 821, 37

Roederer I. U. et al., 2022, ApJS, 260, 27

Roriz M. P., Lugaro M., Pereira C. B., Drake N. A., Junqueira S., Sneden C., 2021a, MNRAS, 501, 5834

Roriz M. P., Lugaro M., Pereira C. B., Sneden C., Junqueira S., Karakas A. I., Drake N. A., 2021b, MNRAS, 507, 1956

Roriz M. P., Pereira C. B., Junqueira S., Lugaro M., Drake N. A., Sneden C., 2023, MNRAS, 518, 5414

Ryabchikova T., Piskunov N., Kurucz R. L., Stempels H. C., Heiter U., Pakhomov Y., Barklem P. S., 2015, Phys. Scr, 90, 054005

Shejeelammal J., Goswami A., Goswami P. P., Rathour R. S., Masseron T., 2020, MNRAS, 492, 3708

Siqueira Mello C. et al., 2013, A&A, 550, A122

Smiljanic R., Porto de Mello G. F., da Silva L., 2007, A&A, 468, 679

Sneden C. A., 1973, PhD thesis, University of Texas, Austin

Sneden C., Bean J., Ivans I., Lucatello S., Sobeck J., 2012, MOOG: LTE line analysis and spectrum synthesis, Astrophysics Source Code Library. record (ascl:1202.009)

Straniero O., Gallino R., Busso M., Chiefei A., Raiteri C. M., Limongi M., Salaris M., 1995, ApJ, 440, L85

Straniero O., Gallino R., Cristallo S., 2006, Nucl. Phys. A, 777, 311

van Aarle E., Van Winckel H., De Smedt K., Kamath D., Wood P. R., 2013, A&A, 554, A106

Van Eck S., Shetye S., Siess L., 2022, Universe, 8, 220

van Raai M. A., Lugaro M., Karakas A. I., García-Hernández D. A., Yong D., 2012, A&A, 540, A44

Yang G.-C. et al., 2016, Res. Astron. Astrophys., 16, 19

APPENDIX A: ABUNDANCE DATA

Table A1. Tungsten elemental abundances derived for the barium giant stars of the program. The targets are listed in the first column. Effective temperature, surface gravity, and metallicity are shown in Columns 2, 3, and 4, respectively. The logarithmic W abundances derived from the W I lines at 4843 and 5224 Å are shown in Columns 5 and 6. The adopted logarithmic abundances and the [W/Fe] ratios, as well as their uncertainties, computed according to Section 3.2, are listed in Columns 7 and 8, respectively. Finally, we show in Column 9, the averaged *s*-process abundances, given by the mean of the [X/Fe] ratios for the elements Sr, Y, Zr, La, Ce, and Nd, reported in Papers I and III.

Star	$T_{\rm eff}$ (K)	$\log g$ (cm s^{-2})	[Fe/H]	W I 4 843 Å	W I 5 224 Å	Adopted	[W/Fe]	[*s*/Fe]
BD−08°3194	4900	3.0	−0.10 ± 0.16	2.01	1.91	1.96 ± 0.25	+1.41 ± 0.30	+1.09 ± 0.11
BD−09°4337	4800	2.6	−0.24 ± 0.21	2.41	2.26	2.34 ± 0.25	+1.93 ± 0.30	+1.42 ± 0.11
BD−14°2678	5200	3.1	+0.01 ± 0.12	...	...	...	...	+0.87 ± 0.10
CD−27°2233	4700	2.4	−0.25 ± 0.18	1.11	1.11	1.11 ± 0.25	+0.71 ± 0.30	+0.88 ± 0.10
CD−29°8822	5100	2.8	+0.04 ± 0.15	1.41	...	1.41 ± 0.30	+0.72 ± 0.35	+0.95 ± 0.10
CD−30°8774	4900	2.3	−0.11 ± 0.14	...	...	...	...	+0.42 ± 0.11
CD−38°585	4800	2.6	−0.52 ± 0.09	1.31	1.61	1.46 ± 0.25	+1.33 ± 0.30	+1.21 ± 0.11
CD−42°2048	4400	1.6	−0.23 ± 0.16	1.41	1.31	1.36 ± 0.33	+0.94 ± 0.37	+1.04 ± 0.11
CD−53°8144	4800	2.3	−0.19 ± 0.15	1.31	1.41	1.36 ± 0.25	+0.90 ± 0.30	+0.85 ± 0.10
CD−61°1941	4800	2.4	−0.20 ± 0.14	1.21	1.41	1.31 ± 0.25	+0.86 ± 0.30	+0.84 ± 0.11
CPD−62°1013	5100	2.6	−0.08 ± 0.14	...	...	...	...	+0.81 ± 0.11
CPD−64°4333	4900	2.6	−0.10 ± 0.18	2.01	2.21	2.11 ± 0.25	+1.56 ± 0.30	+1.22 ± 0.11
HD 4084	4800	2.8	−0.42 ± 0.15	1.11	...	1.11 ± 0.25	+0.88 ± 0.30	+0.81 ± 0.11
HD 5424	4700	2.4	−0.41 ± 0.18	1.61	1.71	1.66 ± 0.25	+1.42 ± 0.30	+1.30 ± 0.11
HD 5825	5000	2.7	−0.48 ± 0.08	...	...	...	...	+0.86 ± 0.10
HD 15589	4900	3.1	−0.27 ± 0.15	1.91	1.91	1.91 ± 0.25	+1.53 ± 0.30	+1.12 ± 0.11
HD 20394	5100	2.9	−0.22 ± 0.12	1.61	1.81	1.71 ± 0.30	+1.28 ± 0.34	+1.15 ± 0.10
HD 21989	4400	1.8	−0.14 ± 0.17	0.91	0.91	0.91 ± 0.33	+0.40 ± 0.37	+0.51 ± 0.11
HD 22285	4900	2.3	−0.60 ± 0.13	1.31	1.46	1.38 ± 0.25	+1.34 ± 0.30	+1.11 ± 0.10
HD 22772	4800	2.4	−0.17 ± 0.13	...	...	...	...	+0.79 ± 0.11
HD 24035	4700	2.5	−0.23 ± 0.15	1.91	1.91	1.91 ± 0.25	+1.49 ± 0.30	+1.36 ± 0.11
HD 29370	4800	2.1	−0.25 ± 0.16	1.61	1.71	1.66 ± 0.25	+1.26 ± 0.30	+0.87 ± 0.11
HD 29685	4900	2.7	−0.07 ± 0.14	...	...	...	...	+0.55 ± 0.10
HD 30240	5100	2.7	+0.02 ± 0.15	...	...	...	...	+0.66 ± 0.10
HD 30554	4800	2.5	−0.12 ± 0.14	1.11	...	1.11 ± 0.25	+0.58 ± 0.30	+0.69 ± 0.10
HD 32712	4600	2.1	−0.24 ± 0.16	1.31	1.41	1.36 ± 0.33	+0.95 ± 0.37	+0.82 ± 0.11
HD 32901	4400	1.6	−0.44 ± 0.14	0.96	1.11	1.03 ± 0.33	+0.82 ± 0.37	+0.54 ± 0.11
HD 35993	5100	2.9	−0.05 ± 0.12	1.61	...	1.61 ± 0.30	+1.01 ± 0.34	+0.99 ± 0.10
HD 36650	4800	2.3	−0.28 ± 0.13	...	...	...	...	+0.57 ± 0.10
HD 38488	4400	2.0	+0.05 ± 0.10	1.11	1.01	1.06 ± 0.33	+0.36 ± 0.37	+0.76 ± 0.11
HD 40430	4900	2.5	−0.23 ± 0.13	...	...	...	...	+0.71 ± 0.10
HD 43389	4500	1.5	−0.50 ± 0.17	1.71	1.81	1.76 ± 0.33	+1.61 ± 0.37	+1.27 ± 0.11
HD 51959	5000	3.2	−0.10 ± 0.15	...	...	...	...	+0.76 ± 0.10
HD 58368	5000	2.6	+0.04 ± 0.14	...	...	...	...	+0.71 ± 0.10
HD 59852	5000	2.2	−0.22 ± 0.10	...	...	...	...	+0.33 ± 0.10
HD 61332	4700	2.1	+0.07 ± 0.13	1.11	...	1.11 ± 0.25	+0.39 ± 0.30	+0.40 ± 0.11
HD 64425	4900	2.4	+0.06 ± 0.16	1.61	1.61	1.61 ± 0.25	+0.90 ± 0.30	+0.88 ± 0.10
HD 66291	4600	1.5	−0.31 ± 0.15	...	...	...	...	+0.66 ± 0.11
HD 67036	4300	1.5	−0.41 ± 0.13	1.06	1.11	1.09 ± 0.33	+0.85 ± 0.37	+0.90 ± 0.11

Table A1 – *continued*

Star	T_{eff} (K)	log g (cm s^{-2})	[Fe/H]	log ϵ(W) W I 4 843 Å	W I 5 224 Å	Adopted	[W/Fe]	[s/Fe]
HD 71458	4600	2.2	-0.03 ± 0.10	1.11	1.11	1.11 ± 0.33	$+0.49 \pm 0.37$	$+0.61 \pm 0.11$
HD 74950	4200	1.2	-0.21 ± 0.13	0.96	1.11	1.03 ± 0.33	$+0.59 \pm 0.37$	$+0.61 \pm 0.12$
HD 82221	4400	1.6	-0.21 ± 0.18	1.01	1.11	1.06 ± 0.33	$+0.62 \pm 0.37$	$+0.79 \pm 0.11$
HD 83548	5000	2.4	$+0.03 \pm 0.14$	...	...	...	...	$+0.62 \pm 0.11$
HD 84610	4900	2.5	$+0.00 \pm 0.14$	...	...	...	...	$+0.54 \pm 0.11$
HD 84678	4600	1.7	-0.13 ± 0.16	1.91	1.71	1.81 ± 0.33	$+1.29 \pm 0.37$	$+1.31 \pm 0.11$
HD 88035	4900	2.4	-0.10 ± 0.18	1.46	1.71	1.59 ± 0.25	$+1.04 \pm 0.30$	$+0.95 \pm 0.10$
HD 88562	4300	1.6	-0.27 ± 0.15	...	1.21	1.21 ± 0.33	$+0.83 \pm 0.37$	$+0.84 \pm 0.11$
HD 89175	4900	2.1	-0.55 ± 0.13	1.61	1.91	1.76 ± 0.25	$+1.66 \pm 0.30$	$+1.36 \pm 0.11$
HD 91208	5100	3.0	$+0.05 \pm 0.14$	...	...	...	...	$+0.77 \pm 0.11$
HD 91979	4900	2.7	-0.11 ± 0.12	1.11	...	1.11 ± 0.25	$+0.57 \pm 0.30$	$+0.80 \pm 0.11$
HD 92626	4800	2.3	-0.15 ± 0.22	2.21	2.36	2.28 ± 0.25	$+1.78 \pm 0.30$	$+1.38 \pm 0.11$
HD 105902	4700	2.4	-0.18 ± 0.17	1.71	1.61	1.66 ± 0.25	$+1.19 \pm 0.30$	$+1.20 \pm 0.11$
HD 107264	4500	1.5	-0.19 ± 0.17	1.56	1.46	1.51 ± 0.33	$+1.05 \pm 0.37$	$+0.88 \pm 0.11$
HD 107541	5000	3.2	-0.63 ± 0.11	2.01	2.15	2.08 ± 0.30	$+2.06 \pm 0.34$	$+1.59 \pm 0.11$
HD 110483	4900	2.6	-0.04 ± 0.14	1.36	...	1.36 ± 0.25	$+0.75 \pm 0.30$	$+0.86 \pm 0.11$
HD 110591	4700	1.8	-0.56 ± 0.12	...	...	...	...	$+0.60 \pm 0.10$
HD 111315	4900	2.0	$+0.04 \pm 0.09$	...	...	...	...	$+0.50 \pm 0.11$
HD 113291	4700	2.6	-0.02 ± 0.16	1.46	...	1.46 ± 0.25	$+0.83 \pm 0.30$	$+0.96 \pm 0.11$
HD 116869	4800	2.3	-0.36 ± 0.12	...	...	...	...	$+0.76 \pm 0.11$
HD 119185	4800	2.0	-0.43 ± 0.10	...	...	...	...	$+0.38 \pm 0.10$
HD 120571	4600	1.7	-0.39 ± 0.09	0.81	0.91	0.86 ± 0.33	$+0.60 \pm 0.37$	$+0.56 \pm 0.11$
HD 120620	5000	3.3	-0.14 ± 0.18	2.01	2.01	2.01 ± 0.30	$+1.50 \pm 0.35$	$+1.37 \pm 0.10$
HD 122687	5000	2.6	-0.07 ± 0.13	1.31	...	1.31 ± 0.30	$+0.73 \pm 0.35$	$+0.93 \pm 0.10$
HD 123396	4600	1.9	-1.04 ± 0.13	0.81	1.21	1.01 ± 0.33	$+1.40 \pm 0.37$	$+0.98 \pm 0.10$
HD 123701	5000	2.5	-0.44 ± 0.09	1.31	1.61	1.46 ± 0.30	$+1.25 \pm 0.34$	$+1.04 \pm 0.10$
HD 123949	4600	2.2	-0.09 ± 0.18	1.86	1.81	1.84 ± 0.33	$+1.28 \pm 0.37$	$+1.21 \pm 0.11$
HD 126313	4900	2.2	-0.10 ± 0.16	1.36	1.71	1.54 ± 0.25	$+0.99 \pm 0.30$	$+0.89 \pm 0.11$
HD 130255	4400	1.5	-1.11 ± 0.11	...	...	...	...	$+0.34 \pm 0.11$
HD 131670	4700	2.2	-0.04 ± 0.15	1.06	...	1.06 ± 0.25	$+0.45 \pm 0.30$	$+0.58 \pm 0.11$
HD 136636	4900	2.5	-0.04 ± 0.18	1.31	1.11	1.21 ± 0.25	$+0.60 \pm 0.30$	$+0.94 \pm 0.10$
HD 142751	4600	2.0	-0.10 ± 0.13	1.06	1.11	1.09 ± 0.33	$+0.54 \pm 0.37$	$+0.69 \pm 0.11$
HD 143899	5000	2.5	-0.27 ± 0.12	...	...	...	...	$+0.72 \pm 0.10$
HD 147884	5100	3.0	-0.09 ± 0.15	...	...	...	...	$+0.86 \pm 0.10$
HD 148177	4400	1.6	-0.15 ± 0.15	0.61	0.81	0.71 ± 0.33	$+0.21 \pm 0.37$	$+0.58 \pm 0.11$
HD 154430	4200	1.2	-0.36 ± 0.19	1.51	1.21	1.36 ± 0.33	$+1.07 \pm 0.37$	$+1.07 \pm 0.11$
HD 162806	4500	1.7	-0.26 ± 0.17	0.96	1.11	1.03 ± 0.33	$+0.64 \pm 0.37$	$+0.78 \pm 0.11$
HD 168214	5300	3.2	-0.08 ± 0.10	...	...	...	...	$+0.92 \pm 0.10$
HD 168560	4400	1.6	-0.13 ± 0.13	0.86	1.01	0.94 ± 0.33	$+0.42 \pm 0.37$	$+0.45 \pm 0.11$
HD 168791	4400	1.7	-0.23 ± 0.17	1.31	1.41	1.36 ± 0.33	$+0.94 \pm 0.37$	$+0.81 \pm 0.11$
HD 176105	4500	1.6	-0.14 ± 0.12	0.76	1.01	0.88 ± 0.33	$+0.38 \pm 0.37$	$+0.48 \pm 0.11$
HD 177192	4700	1.7	-0.17 ± 0.20	...	...	...	...	$+0.53 \pm 0.10$
HD 180996	4900	2.6	$+0.06 \pm 0.15$	...	...	...	...	$+0.52 \pm 0.11$
HD 182300	5000	2.7	$+0.06 \pm 0.16$	1.31	...	1.31 ± 0.30	$+0.60 \pm 0.35$	$+0.87 \pm 0.10$
HD 183915	4500	1.6	-0.39 ± 0.14	1.31	1.36	1.34 ± 0.33	$+1.08 \pm 0.37$	$+1.00 \pm 0.11$
HD 187308	4900	2.5	-0.08 ± 0.11	...	...	...	...	$+0.63 \pm 0.11$
HD 193530	4400	1.6	-0.17 ± 0.14	...	...	...	...	$+0.57 \pm 0.11$
HD 196445	4400	1.4	-0.19 ± 0.17	1.51	1.41	1.46 ± 0.33	$+1.00 \pm 0.37$	$+1.03 \pm 0.11$
HD 199435	5000	2.6	-0.39 ± 0.12	1.41	1.71	1.56 ± 0.30	$+1.30 \pm 0.34$	$+1.07 \pm 0.10$
HD 200995	4600	2.1	-0.03 ± 0.17	1.06	1.11	1.09 ± 0.33	$+0.47 \pm 0.37$	$+0.62 \pm 0.11$
HD 201657	4700	2.2	-0.34 ± 0.17	1.56	1.61	1.59 ± 0.25	$+1.28 \pm 0.30$	$+1.12 \pm 0.11$
HD 201824	4900	2.3	-0.33 ± 0.17	1.41	1.76	1.59 ± 0.25	$+1.27 \pm 0.30$	$+1.14 \pm 0.11$
HD 204075	5300	1.5	$+0.06 \pm 0.17$	...	...	...	...	$+0.89 \pm 0.10$
HD 207277	4600	2.0	-0.13 ± 0.14	1.11	1.11	1.11 ± 0.33	$+0.59 \pm 0.37$	$+0.72 \pm 0.11$
HD 210709	4700	2.6	-0.10 ± 0.14	0.91	...	0.91 ± 0.25	$+0.36 \pm 0.30$	$+0.60 \pm 0.11$
HD 210946	4800	2.1	-0.12 ± 0.13	...	...	...	...	$+0.63 \pm 0.11$
HD 211173	4700	2.3	-0.39 ± 0.09	...	...	...	...	$+0.45 \pm 0.10$
HD 211594	4900	2.4	-0.43 ± 0.14	1.61	1.76	1.68 ± 0.25	$+1.46 \pm 0.30$	$+1.35 \pm 0.10$
HD 211954	4400	1.7	-0.51 ± 0.19	1.91	1.71	1.81 ± 0.33	$+1.67 \pm 0.37$	$+1.28 \pm 0.11$
HD 214579	4400	1.6	-0.26 ± 0.14	1.11	1.11	1.11 ± 0.33	$+0.72 \pm 0.37$	$+0.70 \pm 0.11$
HD 217143	4600	2.1	-0.35 ± 0.17	1.11	1.11	1.11 ± 0.33	$+0.81 \pm 0.37$	$+0.88 \pm 0.11$
HD 217447	5000	2.5	-0.17 ± 0.11	...	...	...	...	$+0.85 \pm 0.10$
HD 219116	4900	2.3	-0.61 ± 0.09	...	...	...	...	$+0.85 \pm 0.11$

Table A1 – *continued*

Star	$T_{\rm eff}$ (K)	log g (cm s^{-2})	[Fe/H]	W I 4 843 Å	W I 5 224 Å	Adopted	[W/Fe]	[s/Fe]
HD 223586	4700	2.9	−0.08 ± 0.11	1.21	...	1.21 ± 0.25	+0.64 ± 0.30	+0.83 ± 0.11
HD 223617	4700	2.3	−0.18 ± 0.13	1.01	...	1.01 ± 0.25	+0.54 ± 0.30	+0.67 ± 0.11
HD 252117	4600	1.8	−0.14 ± 0.19	1.41	1.41	1.41 ± 0.33	+0.90 ± 0.37	+0.95 ± 0.11
HD 273845	4800	2.5	−0.15 ± 0.16	1.61	1.61	1.61 ± 0.25	+1.11 ± 0.30	+1.03 ± 0.10
HD 288174	4800	2.3	−0.05 ± 0.15	1.21	...	1.21 ± 0.25	+0.61 ± 0.30	+0.68 ± 0.10
MFU 112	4900	2.4	−0.43 ± 0.15	1.86	2.06	1.96 ± 0.25	+1.74 ± 0.30	+1.33 ± 0.11
BD−18°821	5000	2.3	−0.27 ± 0.15	1.46	1.61	1.54 ± 0.30	+1.16 ± 0.35	+0.87 ± 0.11
CD−26°7844	5100	2.8	+0.02 ± 0.11	...	...	...	...	+0.45 ± 0.10
CD−30°9005	4700	2.3	+0.05 ± 0.12	1.21	1.11	1.16 ± 0.25	+0.46 ± 0.30	+0.62 ± 0.10
CD−34°6139	4900	2.2	−0.07 ± 0.13	...	...	...	...	+0.58 ± 0.11
CD−34°7430	4900	2.6	+0.01 ± 0.14	...	...	...	...	+0.55 ± 0.11
CD−46°3977	4900	2.6	−0.10 ± 0.15	...	...	...	...	+0.65 ± 0.10
HD 18182	4900	2.4	−0.17 ± 0.10	...	...	...	...	+0.41 ± 0.11
HD 18361	4900	2.6	+0.01 ± 0.15	...	...	...	...	+0.40 ± 0.10
HD 21682	5200	2.8	−0.48 ± 0.12	...	...	...	...	+0.66 ± 0.10
HD 26886	5000	2.5	−0.30 ± 0.10	...	...	...	...	+0.56 ± 0.10
HD 31812	5100	2.6	−0.07 ± 0.11	...	...	...	...	+0.58 ± 0.10
HD 33709	5000	2.1	−0.20 ± 0.14	...	...	...	...	+0.39 ± 0.10
HD 39778	5000	2.5	−0.12 ± 0.12	...	...	...	...	+0.84 ± 0.10
HD 41701	5000	2.6	+0.02 ± 0.13	...	...	...	...	+0.34 ± 0.10
HD 45483	4800	2.2	−0.14 ± 0.12	...	...	...	...	+0.57 ± 0.10
HD 48814	4800	2.3	−0.07 ± 0.11	...	...	...	...	+0.32 ± 0.11
HD 49017	5100	2.8	+0.02 ± 0.11	...	...	...	...	+0.24 ± 0.10
HD 49661	5000	2.4	−0.13 ± 0.10	...	...	...	...	+0.24 ± 0.10
HD 49778	5000	2.3	−0.22 ± 0.12	...	...	...	...	+0.23 ± 0.10
HD 50075	4900	2.5	−0.16 ± 0.11	1.16	...	1.16 ± 0.25	+0.67 ± 0.30	+0.72 ± 0.10
HD 50843	4700	2.3	−0.31 ± 0.13	0.61	...	0.61 ± 0.25	+0.27 ± 0.30	+0.44 ± 0.11
HD 53199	5000	2.3	−0.23 ± 0.13	...	...	...	...	+0.77 ± 0.10
HD 58121	4600	1.8	−0.01 ± 0.13	...	...	...	...	+0.30 ± 0.11
HD 88495	4900	3.0	−0.11 ± 0.10	...	...	...	...	+0.67 ± 0.11
HD 90167	5000	2.6	−0.04 ± 0.11	...	...	...	...	+0.40 ± 0.11
HD 95193	5000	2.7	+0.04 ± 0.12	...	...	...	...	+0.52 ± 0.10
HD 107270	5400	2.7	+0.05 ± 0.17	...	...	...	...	+0.41 ± 0.10
HD 109061	4700	2.0	−0.56 ± 0.09	...	...	...	...	+0.62 ± 0.10
HD 113195	4700	2.1	−0.15 ± 0.12	...	...	...	...	+0.50 ± 0.11
HD 115277	4800	2.4	−0.03 ± 0.15	...	...	...	...	+0.41 ± 0.11
HD 119650	4500	1.6	−0.10 ± 0.13	...	...	...	...	+0.27 ± 0.11
HD 134698	4500	1.7	−0.52 ± 0.12	...	...	...	...	+0.49 ± 0.11
HD 139266	4300	1.5	−0.27 ± 0.18	1.11	1.11	1.11 ± 0.33	+0.73 ± 0.37	+0.81 ± 0.11
HD 139409	4700	2.1	−0.51 ± 0.13	...	...	...	...	+0.47 ± 0.10
HD 169106	4900	2.2	+0.01 ± 0.12	...	...	...	...	+0.36 ± 0.10
HD 184001	5000	2.5	−0.21 ± 0.14	...	...	...	...	+0.59 ± 0.11
HD 204886	4600	2.1	+0.04 ± 0.15	1.31	1.26	1.28 ± 0.33	+0.59 ± 0.37	+0.66 ± 0.16
HD 213084	5000	2.8	−0.09 ± 0.15	1.21	...	1.21 ± 0.30	+0.65 ± 0.35	+0.81 ± 0.10
HD 223938	5000	2.9	−0.42 ± 0.11	...	...	...	...	+0.74 ± 0.10
MFU 214	4800	2.4	+0.00 ± 0.12	...	...	...	...	+0.30 ± 0.11
MFU 229	4900	2.6	−0.01 ± 0.11	...	...	...	...	+0.54 ± 0.10
HD 12392	4900	3.0	−0.08 ± 0.18	1.71	1.81	1.76 ± 0.25	+1.19 ± 0.30	+1.14 ± 0.11
HD 17067	4200	1.1	−0.61 ± 0.21	1.26	1.31	1.28 ± 0.33	+1.25 ± 0.37	+0.94 ± 0.11
HD 90127	4600	2.2	−0.40 ± 0.10	1.06	...	1.06 ± 0.33	+0.81 ± 0.37	+0.79 ± 0.11
HD 102762	4400	1.7	−0.17 ± 0.20	1.66	1.61	1.63 ± 0.33	+1.15 ± 0.37	+1.01 ± 0.11
HD 114678	5200	2.8	−0.50 ± 0.13	1.91	1.71	1.81 ± 0.30	+1.66 ± 0.34	+1.17 ± 0.10
HD 180622	4600	2.2	+0.03 ± 0.12	0.81	...	0.81 ± 0.33	+0.13 ± 0.37	+0.43 ± 0.11
HD 200063	4100	1.1	−0.34 ± 0.20	1.16	1.16	1.16 ± 0.33	+0.85 ± 0.37	+0.83 ± 0.11
HD 210030	4700	1.9	−0.03 ± 0.11	...	...	...	...	+0.31 ± 0.11
HD 214889	4900	2.6	−0.17 ± 0.12	...	...	...	...	+0.58 ± 0.10
HD 215555	5200	3.2	−0.08 ± 0.12	...	...	...	...	+0.84 ± 0.10
HD 216809	4400	1.2	−0.04 ± 0.14	0.91	1.11	1.01 ± 0.33	+0.40 ± 0.37	+0.49 ± 0.11
HD 221879	4300	1.3	−0.10 ± 0.19	1.01	1.11	1.06 ± 0.33	+0.51 ± 0.37	+0.66 ± 0.11
HD 749	4700	2.6	−0.29 ± 0.15	1.16	1.26	1.21 ± 0.25	+0.85 ± 0.30	+0.89 ± 0.11
HD 88927	4600	2.3	+0.02 ± 0.13	...	...	...	...	+0.33 ± 0.11
BD+09°2384	4900	2.5	−0.98 ± 0.10	...	...	...	...	+0.72 ± 0.11
HD 89638	4900	2.4	−0.19 ± 0.11	...	...	...	...	+0.57 ± 0.10

Table A1 – *continued*

Star	T_{eff} (K)	$\log g$ (cm s^{-2})	[Fe/H]	$\log \epsilon(\text{W})$			[W/Fe]	[*s*/Fe]
				W I 4 843 Å	W I 5 224 Å	Adopted		
HD 187762	4800	2.4	-0.30 ± 0.11	...	...	...	...	$+0.40 \pm 0.11$
NGC 5822-201	5200	2.7	-0.11 ± 0.10	...	...	...	...	$+0.80 \pm 0.10$
NGC 5822-2	5100	2.4	-0.15 ± 0.09	...	...	...	...	$+0.75 \pm 0.10$
HD 10613	4950	2.7	-0.92 ± 0.12	1.11	1.11	1.11 ± 0.25	$+1.38 \pm 0.30$	$+1.25 \pm 0.11$
CD$-25°6606$	5300	2.7	$+0.12 \pm 0.14$	...	...	...	...	$+0.58 \pm 0.11$
HD 46040	4800	2.4	$+0.11 \pm 0.13$	1.61	1.61	1.61 ± 0.25	$+0.83 \pm 0.30$	$+0.97 \pm 0.11$
HD 49841	5200	3.2	$+0.21 \pm 0.13$	...	...	...	...	$+0.68 \pm 0.10$
HD 82765	5100	2.6	$+0.19 \pm 0.10$	...	...	...	...	$+0.30 \pm 0.11$
HD 84734	5200	2.9	$+0.20 \pm 0.12$	...	...	...	...	$+0.60 \pm 0.10$
HD 85205	5300	2.8	$+0.23 \pm 0.16$	...	...	...	...	$+0.60 \pm 0.11$
HD 101079	5000	2.7	$+0.10 \pm 0.12$	...	...	...	...	$+0.46 \pm 0.10$
HD 130386	4900	2.7	$+0.16 \pm 0.13$	...	...	...	...	$+0.48 \pm 0.11$
HD 139660	5000	2.8	$+0.26 \pm 0.14$	...	...	...	...	$+0.47 \pm 0.11$
HD 198590	5100	2.6	$+0.18 \pm 0.14$	...	...	...	...	$+0.42 \pm 0.10$
HD 212209	4700	2.4	$+0.30 \pm 0.13$	...	...	...	...	$+0.25 \pm 0.11$

This paper has been typeset from a TEX/LATEX file prepared by the author.